

Mechanical stratigraphy in the western equatorial region of Mars based on thrust fault–related fold topography and implications for near-surface volatile reservoirs

Chris H. Okubo[†]

Richard A. Schultz

Geomechanics–Rock Fracture Group, Department of Geological Sciences, Mackay School of Earth Sciences and Engineering, University of Nevada, Reno, Nevada 89557-0138, USA

ABSTRACT

Variations in lithology and pore-volatile pressure influence the distribution of layer and interface strength (mechanical stratigraphy) within the crust. In this paper, we show how mechanical stratigraphy can be inferred from the topography of thrust fault–related folds. A thrust fault propagating upward through mechanically well-stratified crust induces the nucleation of secondary backthrust faults. Because such backthrusts are not predicted (and do not occur) in mechanically homogeneous crust, the presence of backthrusts can be used to map variations in the mechanical strength of the crust (e.g., bedding planes, volatile-saturated reservoirs). Dip directions of faults indicate the presence of strength discontinuities within thrust-related folds. We show that the slopes of fault-related fold limbs are reliable indicators of fault-dip direction. We then apply this slope-asymmetry approach to thrust-related folds on Mars. We find that thrust-related folds that have secondary backthrusts are spatially correlated with a general lithologic sequence of lava flows overlying older impact ejecta and young lobate ejecta craters on the lava-flow surface—evidence of near-surface volatiles such as water ice. We demonstrate that secondary backthrusts within fault-related folds in the western equatorial region of Mars formed because of volatile-enhanced mechanical stratification of lava-flow and ejecta lithologic sequences.

Keywords: thrust fault, wrinkle ridge, to-

pography, mechanical stratigraphy, fluid flow, Mars tectonics.

INTRODUCTION

Field observations (King and Yielding, 1984; Stone, 1999), kinematic models (Suppe, 1985; Mercier et al., 1997), and numerical models (Stein and Ekström, 1992; Cooke and Pollard, 1997; Fig. 1) show that folds around thrust faults are asymmetric in profile. The fold limb ahead of the upper thrust-fault tip (the forelimb) is steeper than the limb above the deeper sections of the thrust (the backlimb; Fig. 1). Accordingly, the asymmetry in fold-limb slope correlates with the dip direction of the subjacent thrust fault. That is, the thrust fault is shallowest below the steep forelimb and dips toward and below the shallower-dipping backlimb. This slope-asymmetry relationship can be used to determine thrust-fault geometries from topography.

In this paper, we propose and validate a method for mapping subjacent fault-dip directions and relative downdip fault lengths from the topography of thrust fault–related folds. We choose to evaluate fold topography because such data are commonly available for terrestrial folds and are the principal (or only) source of structural information for planetary thrust-related folds (Golombek et al., 1991, 2001; Watters and Robinson, 1997; Kreslavsky and Basilevsky, 1998; Bilotti and Suppe, 1999). Planetary landforms termed “wrinkle ridges” (Colton et al., 1972; Hodges, 1973; Howard and Muehlberger, 1973; Young et al., 1973) are commonly inferred to be thrust fault–related folds. As we shall show, fault-dip directions below wrinkle ridges can be used to interpret stratification of materials having varying mechanical strengths within

the shallow Martian crust (e.g., Tanaka et al., 2003; Okubo and Schultz, 2002). The ultimate purpose of this analysis is to infer the presence of near-surface volatile (fluid or ice) reservoirs on the basis of wrinkle-ridge topography.

FAULT DIP AND DEPTH FROM TOPOGRAPHY

Planetary surfaces are cut by numerous fractures, bedding planes, and other mechanical strength discontinuities between blocks of intact rock. The effective strength of the shallow crust is therefore dependent on the strength of intact shallow-crustal rocks combined with the strength of these generally weaker discontinuities. This collection of blocks of intact rock separated by mechanical discontinuities is commonly referred to as a fractured *rock mass* (e.g., Bieniawski, 1989; Bell, 1992; Priest, 1993) to distinguish the large-scale mechanical behavior of the shallow crust from the small-scale behavior of intact rock. This study investigates the large-scale behavior of the shallow Martian crust at the scale where both intact rock and discontinuity strength are important. Therefore, we proceed with a brief introduction to rock-mass strength and deformability criteria.

Rock-mass strength is commonly quantified by using the rock-mass rating (RMR) system, which is based on peak rock-mass strength determination at failed mines, tunnels, and natural and engineered slopes (Bieniawski, 1978, 1989). As its name implies, this system uses a rating scale to quantify fracture density, the strength of the fracture walls and interstitial gouge, pore pressure within the fractures, and the strength of the intact rock. The rating values for each parameter are summed to arrive at an RMR score (S_{RMR}) between zero and

[†]E-mail: chrisko@mines.unr.edu.

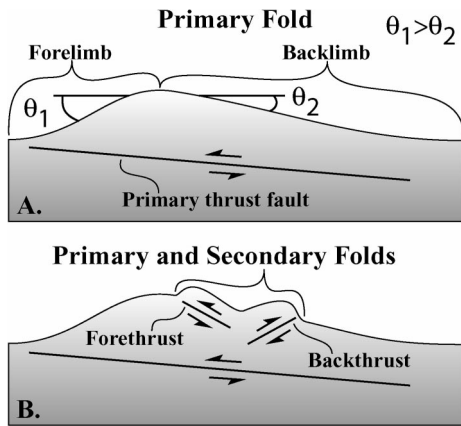


Figure 1. General relationships between thrust-related fold morphology and subjacent thrust-fault geometry. Fold wavelength—the sum of the forelimb and backlimb lengths—is subequal to the length of the subjacent thrust fault as projected to the surface. This thrust is shallowest below the steeper-dipping forelimb and dips toward and below the shallower-dipping backlimb. By using these relationships, the dip direction and relative fault length of (A) a single (primary) thrust, as well as (B) any secondary forethrusts or backthrusts, can be inferred from fold topography.

100; 100 is the strongest, reflecting a low fracture density of <2 fractures per meter, unweathered fracture walls, no interstitial gouge, and no pore pressure. RMR scores are then related to rock-mass strength parameters through empirical relationships (Schultz, 1996; Hoek and Brown, 1997).

The deformation modulus of a rock mass, E^* , analogous to Young's modulus for intact rock (Bieniawski, 1978; Schultz, 1996), is related to S_{RMR} through

$$E^* = 2S_{\text{RMR}} - 100 \quad (1)$$

for values of $S_{\text{RMR}} > 50$ and

$$E^* = 10^{(S_{\text{RMR}} - 10)/40} \quad (2)$$

for $S_{\text{RMR}} < 50$. Increasing pore pressure, as well as increasing fracture density or interstitial gouge content, decreases the S_{RMR} of a rock mass (Bieniawski, 1989) and thereby decreases the magnitudes of E^* . Values of rock-mass Poisson's ratio, ν^* , also decrease with increasing pore pressure (Dvorkin et al., 1999; Wu and Wang, 2001). The range of ν^* is typically between 0.2 and 0.35, whereas E^* generally ranges from 1 GPa to 50 GPa (e.g., Bieniawski, 1978; Hoek and Brown, 1997).

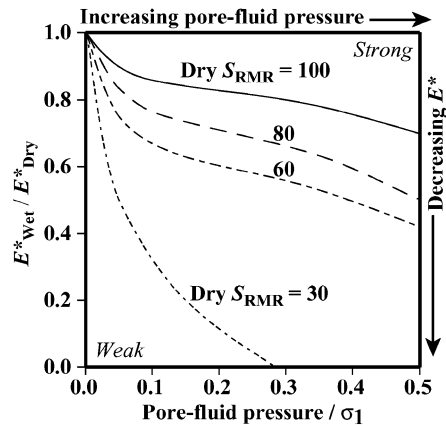


Figure 2. Rock-mass strength, here identified with rock-mass deformation modulus, E^* , decreases with increasing pore pressure for any given initially dry value of S_{RMR} . The relative magnitude of strength reduction is greatest for rock masses with low values dry values of S_{RMR} .

The decrease in E^* with increasing pore pressure is demonstrated in Figure 2. For an initially dry rock mass with S_{RMR} of 30, a 20% increase in the ratio of pore pressure to the maximum principal compressive stress results in a 90% decrease in E^* ; the rock mass loses almost all of its elastic stiffness. Conversely, an initially dry rock mass with an S_{RMR} of 60 loses only 40% of its initial elastic stiffness for the same increase in the pore pressure to compressive stress ratio. Analogous decreases in rock-mass strength parameters such as friction and compressive strength are also predicted. Therefore, increasing pore pressure not only decreases the magnitude of rock-mass shear modulus, but also increases the relative strength contrast between adjacent rock masses that have only slightly different strengths when dry.

Next, we summarize a series of numerical models that demonstrate the sensitivity of fold-limb slopes to reasonable variations in rock-mass deformability, as well as to variations in the dip and depth of the subjacent thrust fault. We use the two-dimensional boundary-element-model FAULT (Schultz and Aydin, 1990; Schultz, 1992; Bruhn and Schultz, 1996; Appendix 1), which uses standard displacement discontinuity equations (Crouch, 1976; Crouch and Starfield, 1983) to calculate the material displacement field around a slipped fault within a fractured rock mass.

The distributions of slip along model faults and weak horizons are calculated in FAULT and are a function of the resolved stress acting

along the fault segments. The tendency for slip is evaluated from the resolved stresses and the frictional and cohesive strength of each segment. The magnitude and distribution of slip are then evaluated on the basis of the deformation modulus of the crust surrounding each slipping segment and the magnitudes of the resolved driving stress. In this way, the magnitude and distribution of slip (and crustal displacements) do not directly constitute a free parameter, but are calculated as elastic displacements around a displacing fracture. Accordingly, the magnitude and distribution of slip and crustal displacements can vary with changes in the strength and deformability of the crust, as well as with changes in fault length and dip and far-field driving stress.

The effects of variations in model parameters on the predicted distribution and magnitude of fault slip and resulting surface displacements (i.e., topography) are modeled by systematically varying either (1) fault dip, depth, or downdip length or (2) rock-mass strength values of friction angle, ϕ^* , Poisson's ratio, ν^* , or deformation modulus, E^* , while holding constant all other variables of fault geometry, material strength, and driving stress (e.g., Schultz and Lin, 2001). The specific effects of changes in crustal strength, fault geometry, and far-field stress on fold topography are detailed in Figure 3. With the elimination of fault-slip magnitude and distribution as a free parameter, the relationships in Figure 3 show that variability in parameters that do affect fault slip (and thereby fold topography) do not drastically affect the principal slope asymmetry. The thrust fault is consistently shallowest below the steep forelimb and dips toward and below the shallower-dipping backlimb in all model variations. Additionally, fold width is subequal to the surface-projected thrust-fault width. In line with field observations and theoretical considerations of brittle-fault strain (Cowie and Scholz, 1992a, 1992b), the FAULT-predicted maximum fault displacement scales with fault length. Therefore, longer faults have larger maximum fault displacements. A corollary to this result is that longer-wavelength folds have greater maximum thrust-fault offsets.

Therefore, although numerical inversions of topography can yield nonunique solutions of fault geometry, the general relationships between fold morphology and fault geometry that are the bases of the slope-asymmetry technique remain viable under reasonable variations of the free parameters that achieve the predicted fault-slip distribution and fold topography. Thus, we conclude that (1) fault-dip direction can be reasonably determined from

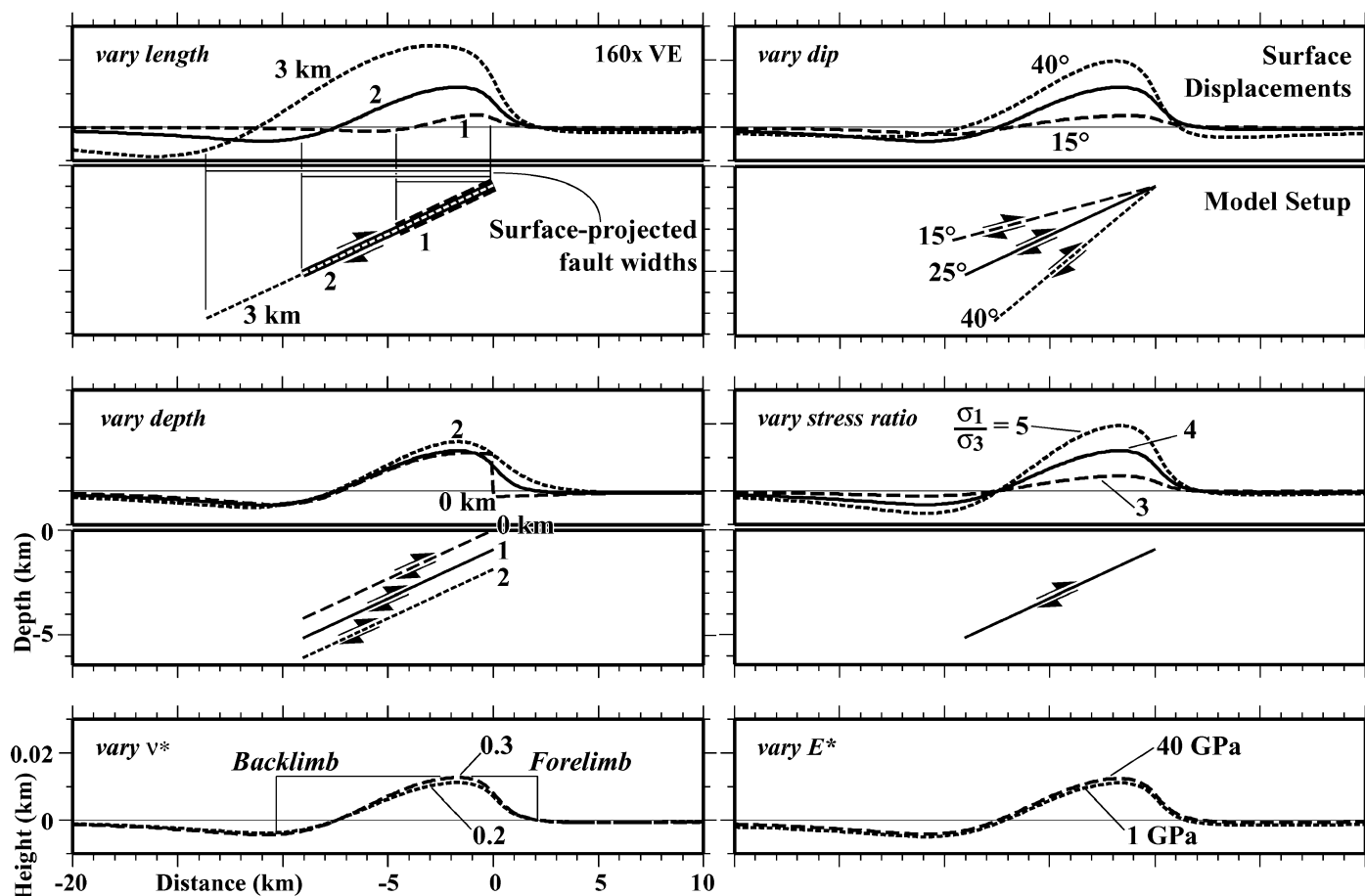


Figure 3. Sensitivity of a fold's slope asymmetry under varying fault and material parameters. Slope-asymmetry relationships, as shown in Figure 1, remain valid for a reasonable range of thrust-fault-dip angles and common material properties.

topography when slope asymmetry can be measured beyond uncertainty in topographic data, and (2) relative downdip fault lengths can be approximated by fold wavelength.

APPROACH

Mechanical stratigraphy describes the spatial distribution of rock-mass strength and deformability (Corbett et al., 1987; Peacock and Zhang, 1994; Gross, 1995; Gross et al., 1997). A mechanically well-stratified crust is composed of alternating strong and weak layers or layer interfaces, such as in an interbedded sequence of mechanically strong limestone and weak shale. A mechanically homogeneous stratigraphy has a uniform strength distribution, such as in a thick sequence of sandstone. In addition to changes in lithology, mechanical stratigraphy can also be caused by variability in pore pressure. Elevated pore pressure of volatile species, such as within a confined aquifer, reduces the effective strength of the reservoir rock mass (Hoek, 1983; Byer-

lee, 1990; Dvorkin et al., 1999) and can result in volatile-induced mechanical stratification within a single lithologic unit.

Thrust-fault geometry can be used to characterize mechanical stratification within a thrust-related fold because crustal-strength distribution strongly influences the tendency for thrust-fault propagation and secondary-fault nucleation, as evaluated with Coulomb failure stress change (Roering et al., 1997; Okubo et al., 2001) and the more general Hoek-Brown failure criterion (Hoek, 1983) for fractured rock masses (Okubo and Schultz, 2002; and this paper). Displacement along an upward-propagating thrust fault induces slip along mechanically weak horizons within the overlying crust (Cooke and Pollard, 1997). This process leads to localization of secondary brittle strain (Niño et al., 1998) consistent with, and enhances the tendency for nucleation of (Roering et al., 1997; Appendix 1), secondary backthrust faults. Furthermore, numerical models demonstrate that in the absence of mechanically weak horizons, the

thrust fault can propagate unimpeded to the surface and, what is more significant, the nucleation of secondary backthrusts is not predicted (Appendix 1). Therefore, we propose that a backthrust fault within the fold surrounding a larger primary thrust fault is evidence that the primary thrust intersected a mechanically weak layer or interface during updip propagation. Additionally, we suggest that the depth of this weak horizon coincides with the depth of the intersection between the backthrust and the primary thrust fault.

A secondary backthrust fault can be identified by an antithetic dip direction vs. the dip of the larger primary thrust (Fig. 1), as well as a shorter downdip fault length relative to the primary thrust. The topography of a thrust-related fold containing a secondary backthrust therefore consists of two antiforms of different wavelengths and senses of slope asymmetry. The fold surrounding the primary thrust is manifested at the surface as the longer-wavelength antiform. Superimposed on this primary antiform is the shorter-wavelength an-

tiform of the fold surrounding the shorter secondary backthrust. The secondary antiform would have an opposite sense of slope asymmetry to that of the primary antiform, reflecting its antithetic dip to the primary thrust. In this way, secondary backthrust faults can be deduced from thrust-related fold topography and thereby lead to interpretations of adjacent mechanical stratigraphy.

Mars Topographic Data

Martian thrust-related folds are especially suited to topographic analyses owing to minimal erosion of the anticlinal fold surface, minimal sediment cover, and surface exposures that are unobstructed by vegetation. Additionally, thrust-related folds are distributed across the entire planet, within terranes of diverse origin and geologic history. The lithologic and volatile-induced variations that are interpretable from mechanical stratigraphy provide an important link between observable wrinkle-ridge topography and the subsurface geology of the Martian crust.

Slope-asymmetry analysis relies upon accurate, high-spatial-resolution topography of thrust-related anticlines. Such data are currently available on a global scale for Mars via the Mars Orbiter Laser Altimeter (MOLA) instrument (Zuber et al., 1992) aboard the *Mars Global Surveyor* (MGS) spacecraft (Albee et al., 1998). MOLA data are available as irregularly spaced spot elevations and as continuous surface digital elevation models (DEMs). We have found that the currently available DEMs are too coarse for slope-asymmetry analysis of thrust-related folds, and therefore we made grids of the irregularly spaced spot elevations to create DEMs with resolutions of 200 pixels per degree, or ~ 297 m/pixel at the equator (Appendix 2). These customized DEMs are used as the basis for the following applications.

Slope-Asymmetry Technique

Topographic inversion modeling is commonly used to predict fault-dip angle, fault-dip direction, fault length, and displacement distribution from observations of coseismic displacements (Lin and Stein, 1989; Stein and Ekström, 1992) or topography (Taboada et al., 1993; Schultz and Watters, 2001). In this inversion method, material (i.e., crustal) displacements are calculated around a model fault of prescribed dip and length. Predicted material displacements at the surface are compared with observed topography, and the model fault geometry is iteratively varied until

model surface displacements are consistent with topography. In Earth-based studies of coseismic surface displacements, fault geometries predicted by this method are consistent with the locations of the related earthquake hypocenters (Lin and Stein, 1989; Ekström et al., 1992) and focal mechanisms (Stein and Ekström, 1992).

The method of slope-asymmetry analysis proposed here is an alternative to the topographic inversion method for evaluating the presence of secondary backthrusts in thrust-related folds. The principal advantage of the slope-asymmetry technique is its efficiency in evaluating large data sets. For each topographic inversion profile, tens to hundreds of iterations of fault geometry *and driving stress* must be tested, and each iteration may require 10–20 min or more of preparation and processing time. In a large mapping area where hundreds of profiles may be required, topographic inversion is time-consuming and returns predictions of downdip fault length, far-field stress magnitudes, slip magnitude and distribution, as well as dip angle and dip direction. In contrast, the slope-asymmetry technique requires 1–2 min per profile in order to determine the only two parameters that are required for this analysis: fault-dip directions and relative downdip fault lengths.

Slope-asymmetry analysis is demonstrated on cross-strike topographic profiles extracted along a single thrust-related fold in southeast Solis Planum, in the western equatorial region of Mars (Fig. 4). A total of 10 profiles were constructed along this wrinkle ridge, adjacent to the four representative profiles shown in Figure 4. The six profiles not shown have comparable dip directions and fault lengths as the four shown profiles. These profiles are constructed away from major lava flows and large impact craters, as apparent in *Viking Orbiter* and *Mars Orbiter* Camera imagery; such lava flows and impact craters would obscure the wrinkle-ridge topography. Fold wavelength (i.e., the sum of the forelimb and backlimb widths) is used as a relative scale for the surface-projected width of these faults. Therefore the longest thrust within the fold is interpreted as the primary fault, implying that this fault is the most deeply rooted. Shorter faults are interpreted as secondary thrusts and are characterized as either backthrusts or forethrusts depending on the interpreted dip angle relative to that of the primary thrust.

Our cross-strike profiles reveal two antiforms, each characterized by distinct limbs (Fig. 4). A narrow 7–20-km-wide antiform is observed on, or adjacent to, a broader 20–35-km-wide antiform, consistent with previous

observations of wrinkle ridges (Watters, 1988; Golombek et al., 1991; Watters and Robinson, 1997; Schultz, 2000). We identify this broad antiform as the surface expression of a fold developed above the longer primary fault. The narrow antiform is interpreted to consist of two distinct folds, one surrounding the near-surface upper tip of the primary thrust and one surrounding a secondary fault.

Slopes of the broader, primary fault-related fold, as well as the smaller fold surrounding its upper tip, are steepest on the east-facing limbs and shallowest on the west. Therefore, according to slope-asymmetry relationships, the primary fault is interpreted to be west dipping. In contrast, the slopes of the narrower secondary fault-related fold are steepest on the west-facing limb and shallowest on the east, indicating by slope asymmetry that the adjacent fault is east dipping. This east-dipping secondary fault is antithetic to the west-dipping primary thrust and is therefore interpreted as a secondary backthrust fault, implying the presence of a weak horizon at depth.

Four cross-strike profiles are next evaluated with rigorous topographic inversion modeling using FAULT (Fig. 5). We model the cumulative ground-surface displacements due to slip and local stress change along both the primary and secondary thrusts. Both thrusts slip simultaneously; the local stress change due to slip along the primary thrust influences the magnitude and distribution of resolved stresses acting along the backthrust and vice versa. Stress interactions between both faults are solved iteratively until numerical convergence is achieved.

We find that the FAULT-predicted best-fit thrust geometries for each profile are consistent with the dip directions and relative downdip fault lengths interpreted by slope asymmetry (compare Figs. 4 and 5). The slope-asymmetry technique is also compared to topographic inversion of thrust-related folds in Isidis Planitia and southern Utopia Planitia in eastern equatorial Mars, and we find similar consistent results (Okubo and Schultz, 2003). Therefore, we propose that results of the slope-asymmetry technique are consistent with the results of, and are a viable qualitative alternative to, the more rigorous topographic inversion analysis.

As Figure 5 shows, local stress interaction between the backthrust and primary thrust does not invalidate the slope-asymmetry relationship. The magnitude of resolved local stress change due to slip along a nearby fault is insufficient to result in a significantly different material-displacement distribution. The fold slope is still steepest above the upper

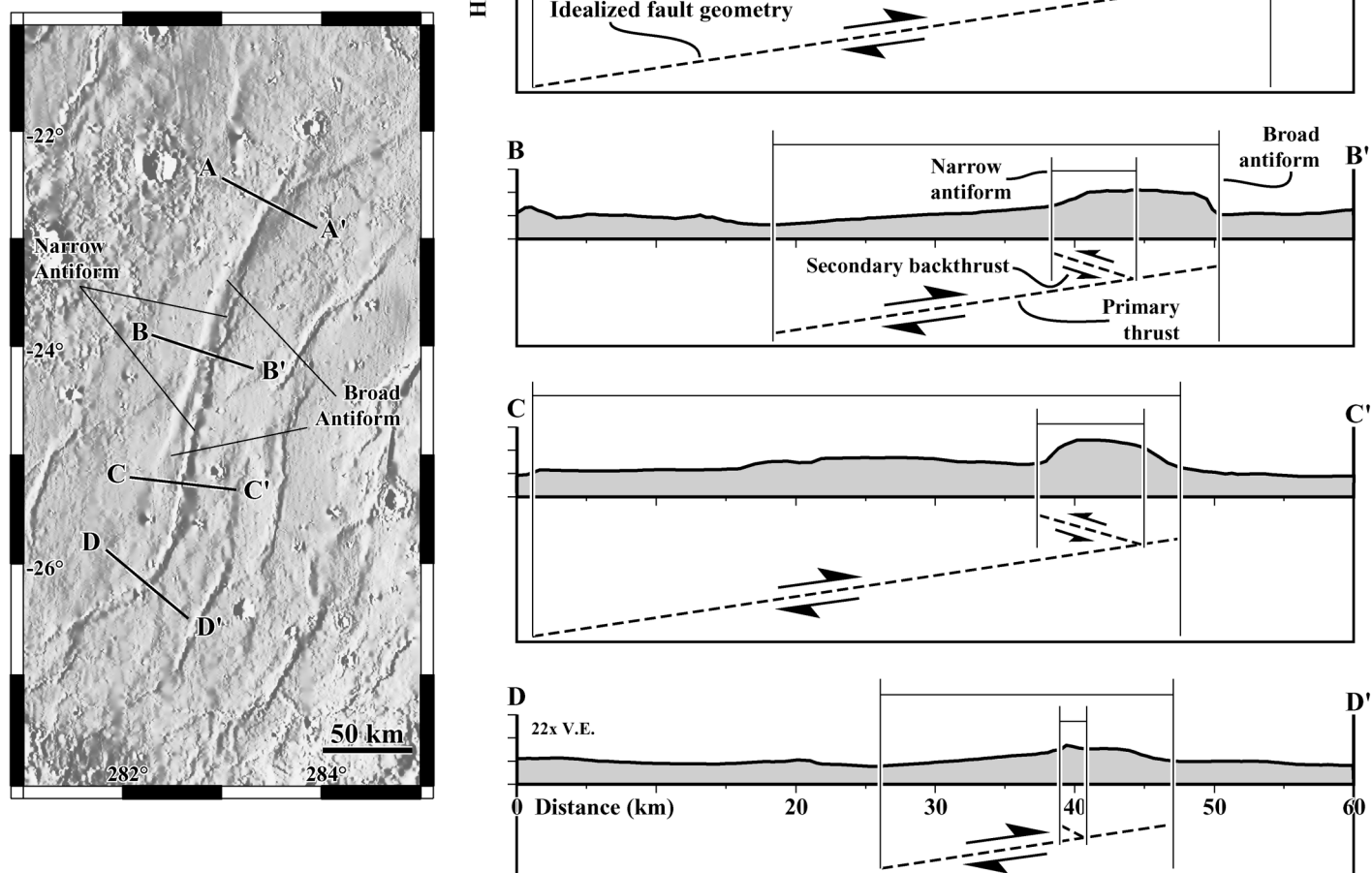


Figure 4. Application of slope-asymmetry analysis to four cross-strike topographic profiles taken along a typical thrust-related fold in southeast Solis Planum, Mars. MOLA-based topography is represented by a solid line with gray undershading, and the general dip directions and lengths of the subjacent thrust fault interpreted from slope asymmetry are shown by dashed lines.

thrust tip and shallower dipping above the deeper parts of the thrust. If the backthrust and primary thrust do not slip simultaneously and offsets along them are separated by a considerable period of time, then interseismic viscoelastic relaxation would dissipate the slip-induced local stress magnitudes to some extent (e.g., Freed and Lin, 1998) and thereby diminish the effect of local stress interaction between the two faults.

APPLICATION

Solis Planum

We next apply slope-asymmetry analysis to a larger area of Solis Planum that includes the demonstration-case wrinkle ridge (Fig. 6A).

Our method of mapping continuous thrust-fault traces from interpretations of fault dip at individual profiles is outlined in Appendix 3. The central and lower regions of the mapped area contain wrinkle ridges that show no topographic evidence of secondary backthrusts, as determined by slope asymmetry. These nonbackthrust folds have either secondary forethrusts (smaller thrusts dipping subparallel with the primary thrust) or have only a primary thrust with no apparent secondary faults. Conversely, the wrinkle ridges along the eastern and western extents of the mapped area show topographic evidence of secondary backthrusts.

Our mapped fault traces are generally consistent with previous mapping efforts (Chicarro et al., 1985; Scott and Tanaka, 1986; Wat-

ters and Maxwell, 1986). What is more significant, however, is that Figure 6B shows for the first time the *dip directions* of these thrust faults and specifically delineates occurrences of secondary backthrust faults. From the mapped distribution of backthrusts, we can now predict the presence of a localized, mechanically weak horizon at depth within the central region of Solis Planum (Fig. 6B). The significance of this weak horizon is discussed in a later section.

West Equatorial Mars

Next, we apply the slope-asymmetry technique to the entire western equatorial region of Mars. Here, we use MOLA-based DEMs having 200 pixels per degree (~ 297 m/pixel

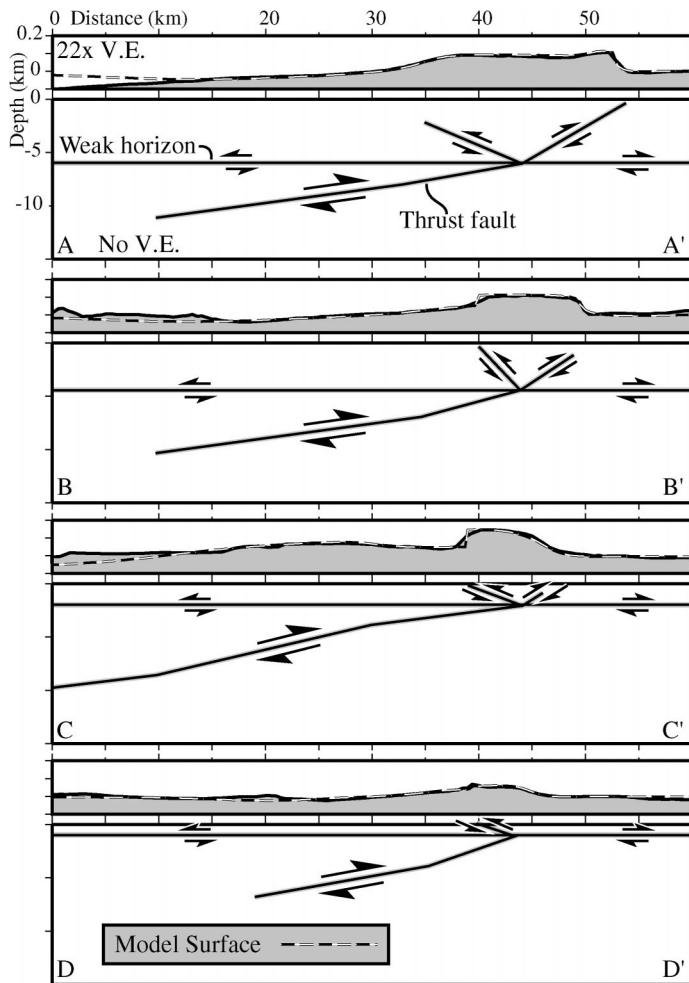


Figure 5. Subjacent thrust-fault geometries predicted by rigorous mechanical modeling of fold topography. Dip directions predicted by slope-asymmetry analysis are consistent with these numerical model predictions of fault-dip direction and relative length.

at the equator) for each Western Hemisphere quadrangle within 65° of the equator (quadrangles defined by Batson et al. (1979)). The resulting interpretations from detailed slope-asymmetry analysis are shown in Figure 7A. For clarity, only representative fault orientations are shown, and fault traces are omitted.

The majority of visible thrust-related folds in western equatorial Mars lack evidence of secondary backthrusts. Thrust-related folds with backthrusts are found to occur only in certain isolated regional patches, such as in Solis and Thaumasia Plana in the east-central region of Figure 7A. On the basis of these findings, we predict that the majority of the western equatorial crust, in which thrust-related folds are found, is mechanically homogeneous (Fig. 7B). Within this broader homogeneous crust, we identify smaller patches of mechanically well-stratified crust. Such patches are found within closed topographic

depressions, such as impact craters or basins, as well as within flat-lying plains, in cratered highlands, and on topographic rises. Further, these well-stratified patches contain at least one localized weak horizon. Some patches contain folds with multiple backthrusts, suggesting multiple weak horizons at depth. These homogeneous and well-stratified characteristics may reach to a depth of 15 km, the average depth of faulting predicted by topographic inversion in the Solis Planum test case.

DISCUSSION

Our mapped distributions of mechanically homogeneous and mechanically well-stratified crust highlight the spatial distribution of weak horizons within the crust. In this section, we correlate our mechanical-stratigraphy map with previous interpretations of lithologic and

pore-volatile distribution in western equatorial Mars. This correlation allows us to investigate the relative mechanical strengths of stacked lithologic units and to demonstrate the contribution of near-surface volatiles to mechanical stratigraphy.

Mechanical Stratigraphy

Our mapped patches of well-defined mechanical stratigraphy may be due in part to specific lithologic variations. Thrust-related folds that have backthrusts occur within units that have been interpreted as lava flows on the basis of observations of lobate flow lobes interspersed with hills containing summit craters, interpreted as possible vent structures by Scott and Tanaka (1986). Furthermore, these surficial lava-flow units consistently overlie units interpreted to consist of impact-crater ejecta. Therefore, we see a spatial correlation of wrinkle-ridge backthrusts with stratigraphic sequences of younger lava flows overlying older ejecta. In most cases, the surficial lava-flow units are Hesperian in age, commonly Hesperian ridged-plains material, and the older ejecta are Noachian basement units. At the Arcadia and Chryse Planitia patches, lava-flow units of both Amazonian and Hesperian age cover older Noachian ejecta. In the Aionia Terra patch, south of Solis Planum (Fig. 7B), there are examples of backthrusts forming in Noachian lava-flow units that overlie Noachian ejecta. Geologic units for these areas are from Scott and Tanaka (1986).

These terranes of lava flows over Noachian basement are not uniquely associated with backthrusts, however. There are regions where the same continuous geologic units associated with backthrusts elsewhere have populations of thrust-related folds that lack backthrusts. Thus, just the contrast between lavas flow and Noachian basement alone may not be great enough to nucleate backthrusts.

Within the lava flow–Noachian basement terranes, impact craters surrounded by lobate ejecta are commonly interspersed among thrust-related folds that have backthrusts (cf. Barlow et al., 2001). Lobate impact-crater ejecta is interpreted to be caused by near-surface volatiles, such as ground water or ice, that were fluidized at impact and mixed in with ejected rock and rock melt (Carr et al., 1977; Mouginiis-Mark, 1979). The entrained volatiles cause the ejected material to be deposited in hummocky, lobate debris flows skirting the impact crater (Stewart et al., 2001; Baratoux et al., 2002). In the absence of entrained volatiles, dry ejecta deposits gradually thin with distance from the crater (Stewart et

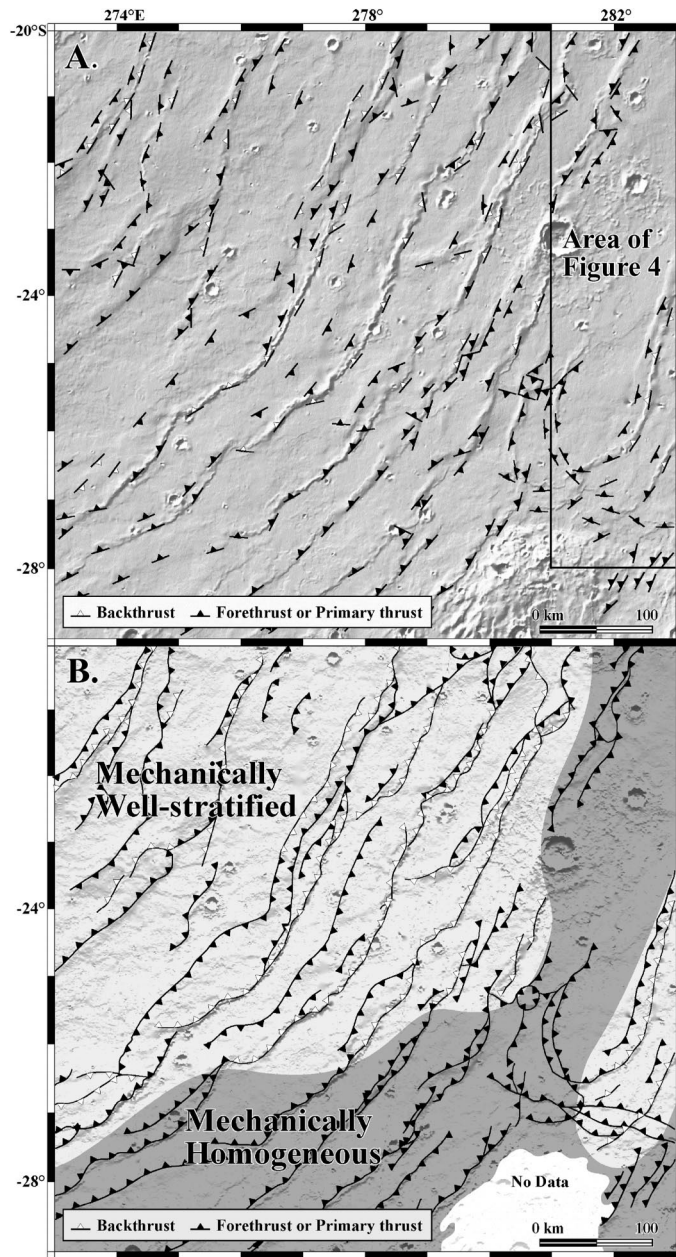


Figure 6. Structural map of southern Solis Planum based on slope-asymmetry analysis of wrinkle-ridge topography. (A) Predictions of fault-dip direction based on analysis of individual cross-strike profiles are linked along strike of the wrinkle ridges to create (B) a map of dip directions of the subjacent thrust fault for the region. Mechanically well-stratified crust is interpreted in areas where wrinkle ridges contain evidence of secondary backthrust faults. See Appendix 3 for details on our mapping approach.

al., 2001). Therefore, lobate ejecta craters are interpreted as evidence of near-surface volatile reservoirs. The spatial correlation of lobate ejecta craters with wrinkle-ridge backthrusts within the key lava flow–Noachian basement (cf. Plate 1 of Barlow et al. [2001] with Fig. 7) terranes suggests that near-surface volatile reservoirs enhance the tendency for the nucleation of wrinkle-ridge backthrusts.

Recent mapping along the equatorial regions of Mars by Barlow et al. (2001) shows a statistically large number of small lobate craters with diameters of <5 km in Solis and Thaumasia Plana. Crater excavation depth has been shown to correlate with crater diameter (Croft, 1980; Garvin et al., 1999), so that smaller craters excavate to shallower depths. Assuming that most of the ejecta are derived

from the top 1/3 of the crater (Melosh, 1989), Barlow et al. predicted volatile reservoirs within 175 m to 240 m of the surface in Solis and Thaumasia Plana. The anomalously large abundance of small lobate craters (and correspondingly shallow excavation depths) suggests that the volatile reservoirs in these plana are at significantly shallower depths than in other equatorial regions that contain lobate craters. Significantly, the mapping results presented here show localized occurrences of secondary backthrusts in Solis and Thaumasia Plana, where Barlow et al. (2001) predicted shallow volatile reservoirs. The correlation of possible near-surface volatile reservoirs and backthrust formation suggests that volatile-induced strength loss may enhance mechanical stratification within western equatorial Mars.

Pore pressure of volatile species—i.e., pore-volatile pressure—can enhance mechanical stratigraphy by preferentially reducing the strength of reservoir host rock (e.g., Fig. 2). Volatile pressure can be driven by a hydrostatic head in the case of fluids or can be caused by the expansion of ice during freezing. Fractured rock masses are natural volatile reservoirs in which volatiles reside within fracture voids and the intragranular pore space of the intact rock (Manzocchi et al., 1998; Indraratna and Ranjith, 2001).

The frictional strength of fracture walls is commonly lower than the strength of the intact rock, and therefore the frictional strength of the fractures largely controls the deformability of the larger rock mass. If Coulomb frictional-sliding conditions are assumed, fracture strength is a function of the cohesion of the fracture walls, C , the friction angle of the wall rock or fill, ϕ^* , the magnitude of pore-volatile pressure within the fracture, P , and the magnitudes of the normal stress, σ_n , and shear stress, τ , acting on the fracture:

$$\tau = C + (\sigma_n - P)\tan \phi^* \quad (3)$$

Pore-volatile pressure within the fracture acts to reduce the magnitude of the effective normal stress acting on the fracture walls. This normal-stress decrease reduces the frictional resistance of the fracture and allows the fracture to slip at a lower magnitude of shear stress than if the fracture was completely dry ($P = 0$). Thus, the presence of pore-volatile pressure reduces the frictional strength of fractures and thereby reduces the strength of the larger rock mass (Bieniawski, 1989).

Interstitial ice can further reduce the strength of a rock mass in a manner similar to that of gouge. Clayey gouge commonly has

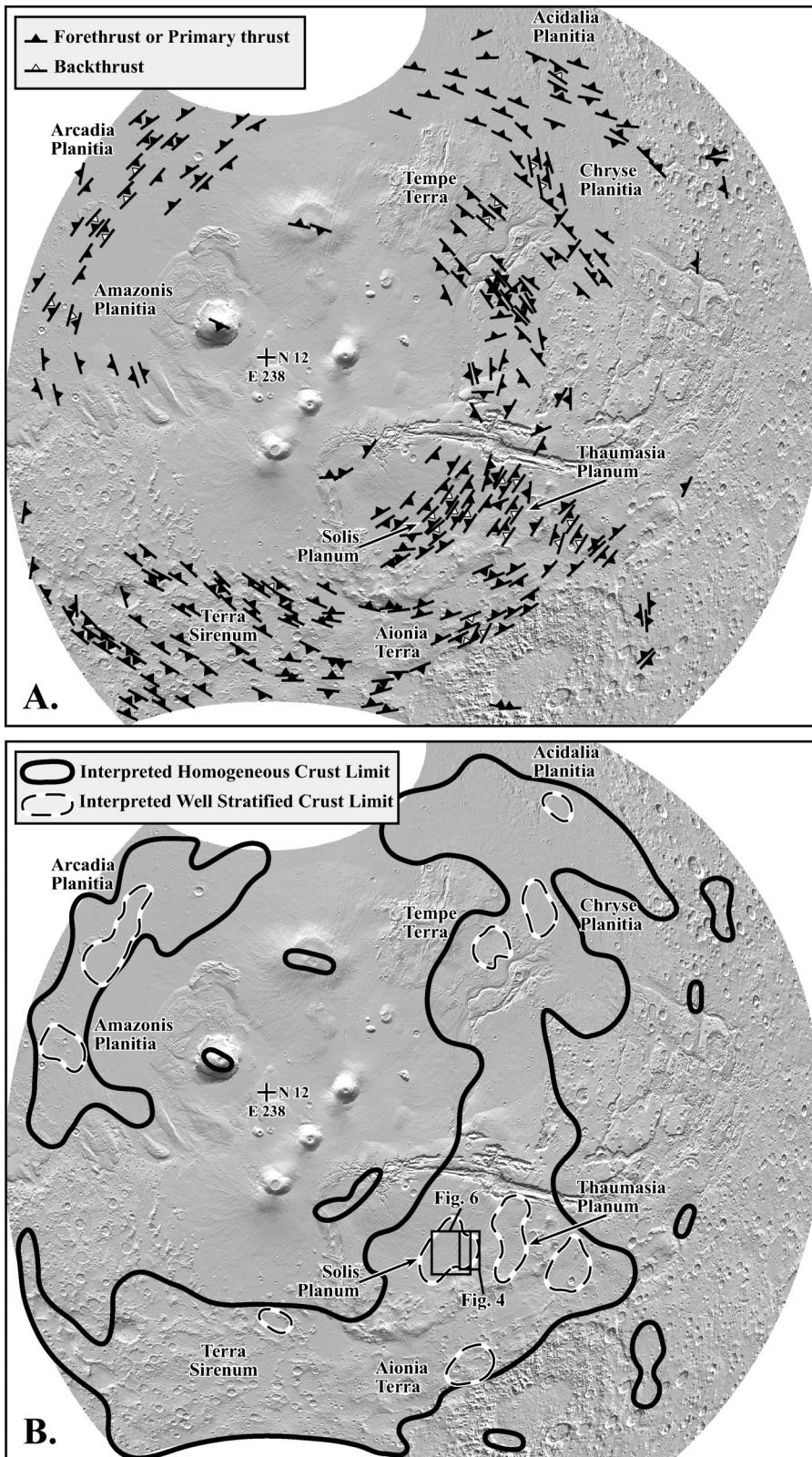


Figure 7. (A) Representative thrust-fault strike and dip directions for wrinkle ridges within the western equatorial region of Mars. (B) Mechanically well-stratified crust is interpreted below patches of wrinkle ridges that have secondary backthrust faults.

friction angles of less than 10° (Saffer et al., 2001; Morrow et al., 2000), which is significantly lower than general friction angles for intact rock (30° – 51° ; Kulhawy, 1975). The presence of frictionally weak gouge can reduce the effective frictional strength of fracture surfaces between blocks of stronger intact rock, leading to lower values of S_{RMR} and resulting in decreased rock-mass strength (Bieniawski, 1989; Hoek and Brown, 1997; Schultz, 1996). In pure water ice, frictional sliding tests yield internal friction angles of $\sim 11^\circ$ under confining pressures of 10–200 MPa (Durham et al., 1983; Beeman et al., 1988). These data suggest that interstitial ice, like gouge, can effectively reduce the strength of fracture surfaces between intact rock blocks and result in decreased rock-mass strength.

The magnitude of volatile-induced strength loss of a rock mass is dependent on the dry strength of the rock mass and is significantly greater for rock masses with inherently low unsaturated strength. Elevated pore-volatile (fluid or ice) pressure can enhance preexisting rock-mass strength contrasts by significantly decreasing the relative strength of layers or layer interfaces that are otherwise only slightly weaker than the surrounding rock when dry. In this way, *increases in a pore-volatile component significantly affect the degree of mechanical stratification within the lava flow–Noachian basement lithologic terranes in western equatorial Mars and thereby enhance the tendency for backthrust nucleation.*

Because the dry (no lobate ejecta) lava flow–Noachian basement terranes have no backthrusts, the contrast in unsaturated rock-mass strength of these layers and their interface is not sufficient to cause one (either a layer or the interface) to act as a relatively weak horizon and nucleate backthrusts. The apparent dependency of backthrust nucleation on elevated pore-volatile pressure suggests that individually, *the lava-flow rock masses and the underlying Noachian sedimentary deposits have only slightly different strengths when dry.* Such a strength condition would prevent the nucleation of backthrusts in the absence of pore-volatile pressure, but would allow for backthrust nucleation, above volatile-induced weak horizons, when saturated. This deduction implies that the ejecta deposits have a strength similar to that of the overlying lava-flow rock mass. It is interesting to note that this statement provides a test of the interpretation that these underlying Noachian deposits consist of impact ejecta.

The frictional strength of granular deposits and poorly indurated sedimentary sequences depends on the clast-size distribution (sort-

ing), packing (porosity), and clast shape. Friction is less than that of intact rock and rock masses for rounded clasts, higher porosity, and uniform clast size. Deposits composed of angular clasts can be as strong as indurated rock masses regardless of clast size and sorting (Mair et al., 2002). As a result, formation and transport mechanisms exert a significant control on the strength and deformability of these materials. In our study area, the apparently approximate equality of the strength of the underlying deposits and that of the younger lava-flow rock mass is thus consistent with the underlying deposits' being composed of angular clasts. High clast angularity is characteristic of locally derived sediment that has undergone minimal transport or reworking, such as the colluvium characteristic of terrestrial impact ejecta (Grant and Schultz, 1993; Urrutia-Fucugauchi et al., 1996; Lilljequist, 2000). Therefore, *the apparent frictional strength of the Noachian basement rocks is consistent with the strength of impact ejecta and supports previous interpretations of these basement rocks.*

Volatile-Rich Décollements

Martian wrinkle ridges have been interpreted as evidence of thin-skinned deformation above volatile-rich décollements on the basis of deflections in observed wrinkle-ridge trends around the peripheries of partially and completely buried impact craters (Allemand and Thomas, 1992; Mangold et al., 1998). These studies propose a primary thrust and secondary backthrust geometry for the subjacent wrinkle-ridge faults. They further suggest that the primary thrust forms because of slip along shallow, subhorizontal, ice-rich décollements within 3 km of the surface.

Alternatively, we suggest that ice- or fluid-rich layers have a secondary role in wrinkle-ridge formation. That is, shallow volatile-rich layers only act to promote secondary backthrust nucleation by reducing rock-mass strength. In the absence of volatile-rich layers, the primary thrust and secondary forethrusts can still form, but only secondary backthrust nucleation is not predicted. Further, our topographic inversion results predict that, instead of being rooted in a shallow décollement, the primary thrust of the test wrinkle ridge of the Solis Planum must be deeply rooted at >10 km depth in order to have surface displacements consistent with observed topography. Thus, *shallow volatile-rich layers enhance the tendency for secondary backthrust nucleation, but are not required for wrinkle-ridge formation.*

CONCLUSIONS

Comparisons with numerical models of displacements around slipped thrust faults demonstrate that the asymmetry in fold-limb slope is a reliable indicator of subjacent fault-dip direction when applied to the topography of thrust-related folds. In addition, the relative downdip length of these faults can be approximated from the wavelength of the overlying fold at the surface. Where secondary backthrust faults are interpreted from slope asymmetry, the crust within the fold can be characterized as being mechanically well-stratified such that the crust contains a mechanically weak horizon at the intersection of the lower backthrust tip and the plane of the larger primary fault. This horizon may be caused by a mechanically weak lithologic layer or layer interface or by pressure-induced strength loss within a volatile reservoir.

When applied to the topography of thrust-related folds on Mars, the physical principles of slope asymmetry and backthrust nucleation at weak horizons suggest distributions of mechanical stratigraphy. On the basis of spatial correlations of interpreted secondary backthrusts in thrust-related folds, previous geologic mapping, and evidence of near-surface volatiles, we propose that the following statements hold true in western equatorial Mars: (1) Thrust-related folds that have backthrusts occur in terranes that have a surficial lava-flow rock mass overlying sediments interpreted to be Noachian basement rocks. (2) The lava-flow rock masses and the underlying Noachian sedimentary deposits have only slightly different mechanical strengths when dry. (3) The apparent strength of the underlying Noachian sediments is consistent with angular impact-derived ejecta colluvium, a finding that supports previous interpretations of these units (e.g., Scott and Tanaka, 1986). (4) Variability in pore-volatile pressure may significantly affect the degree of mechanical stratification within the key lava flow–Noachian basement lithologic terranes. (5) Shallow volatile-rich layers are not required for wrinkle-ridge formation, but only serve to enhance the tendency for secondary backthrust nucleation. (6) The secondary backthrusts and causative primary faults propagated in the presence of near-surface volatiles.

If backthrust nucleation is linked to near-surface volatile reservoirs (as we infer), then thrust-related folds that have backthrusts may be important locales for volatile seeps. Near-surface or surface-breaking faults are prime locations for seeps because these faults act to localize volatile flow, as either conduits (Sib-

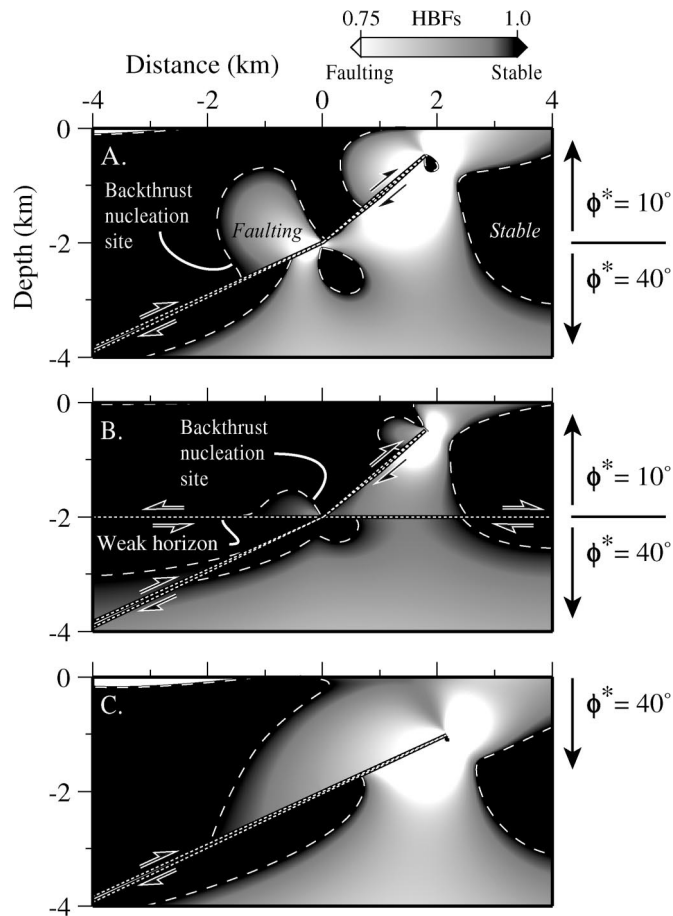
son et al., 1975; Travé et al., 1997; Strayer et al., 2001) or as barriers (Antonellini and Aydin, 1994; Parry, 1998). Furthermore, slip along faults can generate substantial heat (Mase and Smith, 1987; Sleep, 1995), which may act to melt permafrost within adjacent wall rock and potentially lead to volatile release at the surface. Our topographic inversion tests in Solis Planum predict that the subjacent thrusts in fact break the surface. This result means that some thrust-related folds that have backthrusts may have surface-breaking thrusts that crosscut shallow volatile reservoirs (such as in Solis and Thaumasia Plana) and that seeps may occur along the rupture length of these faults. Therefore, detailed remote sensing-based investigations of these backthrust-related fault systems may reveal evidence of volatile release, in the form of springs or seeps.

APPENDIX 1. FAULT-BOUNDARY-ELEMENT MODEL

In FAULT, we model vertical variations in frictional strength as mechanical stratigraphy. Frictional strength variations are represented by vertical changes in fault dip by assuming optimally oriented thrust faults (Jaeger and Cook, 1979) within an Andersonian stress state (Anderson, 1951) and minimal local stress rotation. Aside from friction angle, the model rock-mass boundary elements have otherwise uniform properties such that $E^* = 20$ GPa and $\nu^* = 0.25$. This rock-mass value of E^* corresponds to $S_{\text{RM}} = 64$, consistent with an unweathered to moderately weathered, average-quality rock mass (Hoek and Brown, 1997). Fault elements have $E^* = 20$ GPa, $\nu^* = 0.25$, cohesion $C = 0.3$ MPa, friction angle $\phi^* = 20^\circ$. Weak horizon elements (where present) have $E^* = 3$ GPa, $\nu^* = 0.25$, cohesion $C = 0.3$ MPa, friction angle $\phi^* = 20^\circ$. The magnitude of the far-field driving stress is prescribed to correspond to a uniform principal stress ratio of 4.5, under a half-space boundary condition, and the least compressive principal stress is equal to lithostatic load, if a crustal density of 2600 kg/m³ is assumed. Thus, the magnitudes of these principal stresses are depth dependent.

By using these model boundary conditions, Hoek-Brown stress states for model thrust-related folds are calculated in cross-strike profile and mapped as factors of safety. Hoek-Brown predicts the failure stresses required to nucleate faulting within a fractured rock mass (Hoek and Brown, 1980, 1997) and is similar in form to the Coulomb failure criterion for intact rock (e.g., Schultz, 1996). The Hoek-Brown factor of safety (F_{HB}) is the ratio of the frictional and cohesive strength of the rock mass to the maximum effective principal compressive stress. Accordingly, faulting is predicted where the factor of safety is <1.

The distribution of F_{HB} is first calculated for the case of a mechanically stratified crust, where a weak surface layer overlies a relatively stronger basement. In an Andersonian stress state for thrust faulting, where the maximum compressive stress acts in the horizontal direction, the dip of optimally oriented thrust faults is equal to the rock-mass friction angle (e.g., Jaeger and Cook, 1979). Accordingly,



Appendix Figure 1. Predicted distribution of F_{HB} for model cases with (A) a welded mechanical layer interface at 2 km depth, (B) a frictionally slipping weak horizon at a mechanical layer interface at 2 km depth, and (C) a mechanically homogeneous model crust. Faulting is predicted where F_{HB} values are $F_{HB} < 1$. In A and B, secondary backthrust faulting is predicted to nucleate within lobes of F_{HB} values of $F_{HB} < 1$ that are elongate antithetic to the thrust fault.

thrust faults within the upper 2 km of the model dip at 10° , corresponding to a friction angle of 10° for the upper layer. Faults within the model crust below 2 km dip at 40° , corresponding to a friction angle of 40° for the underlying basement.

The interface between the frictionally weaker upper layer and the underlying basement is first modeled without a frictionally slipping weak horizon. Effectively, these two units have a welded contact. Results of this model show that where the upper tip of an upward-propagating thrust intersects and crosscuts a welded mechanical layer interface, a lobe of F_{HB} values of < 1 localizes above the intersection of the thrust and weak layer (Appendix Fig. 1A). This lobe is elongate antithetic to the dip direction of the thrust fault. Additionally, F_{HB} values of $\ll 1$ are concentrated along the major axis of this lobe and in proximity to the weak layer/thrust fault intersection. Under the prescribed Andersonian stress regime, faulting within this failure lobe will have thrust displacements, and a thrust fault is most likely to nucleate where F_{HB} values are $\ll 1$. Therefore, secondary thrust faulting is predicted above and behind (within the hanging wall of) the upper tip of the initial, primary thrust where it intersects

a weak layer. On the basis of the antithetic orientation of the failure lobe, we interpret the nucleation of a secondary *backthrust* fault within the hanging wall of the primary thrust.

Next, a weak horizon interface is added between the upper and lower mechanical layers, at 2 km depth, while maintaining the same fault geometry as shown in Appendix Figure 1A. A distribution of F_{HB} similar to the welded contact model (Appendix Fig. 1A) is predicted around an upward-propagating thrust that crosscuts a frictionally slipping weak horizon at a mechanical layer interface (Appendix Fig. 1B). With a frictionally slipping weak horizon, the antithetic lobe of F_{HB} values that are < 1 is less areally extensive than in the welded-contact geometry, but is still prominently elongate antithetically away from the intersection of the thrust and mechanical layer interface. Again, we predict the development of a secondary backthrust fault within this unstable lobe.

Finally, a mechanically homogeneous crust is modeled with a thrust-fault dip corresponding to a uniform rock-mass friction angle of 40° and no weak horizon. These results show that in the absence of a mechanical layer interface, antithetic

lobes of F_{HB} values of < 1 are not predicted (Appendix Fig. 1C). Thus, secondary backthrust faulting is also not predicted around the primary thrust in the absence of a mechanical layer interface.

The general prediction of lobes of F_{HB} values that are < 1 antithetic to the intersection between the primary thrust and mechanical layer interface also occurs where the overlying layer is stronger than the layer below 2 km (i.e., where the shallow layer has an internal friction angle of 60° and the deeper layer has a friction angle of 40°). From these model predictions, we infer that a secondary backthrust fault within the fold surrounding a larger primary thrust is evidence that the primary thrust intersected a mechanical layer interface during updip propagation and that the intersection of the backthrust with the primary thrust corresponds to the depth of the mechanical layer interface.

APPENDIX 2. MOLA-BASED DEMS

MOLA Precision Experiment Data Records (PEDRs) comprise spot elevations taken every 300 m along the MGS ground track; each datum is the average surface elevation within a 168-m-diameter footprint (Smith et al., 1999a). Comparisons between coincident range measurements show that the MOLA elevations are accurate to 1 m (Neumann et al., 2001), and the geographic locations of each datum have uncertainties of ~ 30 m radially (Smith et al., 1999a). Therefore, these data provide detailed topographic data of Martian thrust-related anticlines, which are commonly hundreds of kilometers long, tens of kilometers wide, and hundreds of meters high (Chicarro et al., 1985; Watters 1988; Golombek et al., 1991; Watters and Robinson, 1997).

Elevation profiles constructed from individual along-track PEDR data are used to characterize wrinkle-ridge topography. The MGS ground track, however, commonly lies oblique to the trend of the wrinkle ridges (or any other linear structures). This obliquity is a significant difficulty in using the along-track PEDR data to obtain elevation profiles that are optimally oriented subperpendicular to the trend of the wrinkle ridge. Therefore, where wrinkle ridge-perpendicular PEDR profiles are not available, elevation profiles can be constructed from continuous-surface PEDR-based DEMs.

Coincident profiles from DEMs of various resolutions have shown that sampling intervals of less than ~ 100 pixels per degree (~ 600 m/pixel at the equator) do not adequately characterize fold-limb slopes because wrinkle-ridge forelimbs are commonly less than 4 km wide. High spatial resolution (< 300 m/pixel) is required to resolve the slopes of these narrower fold limbs.

High-resolution digital elevation models of the study area were constructed from PEDR data released as of August 2001 (available at <http://wufs.wustl.edu/missions/mgs/mola>). These DEMs were gridded to a resolution of 200 pixels per degree (~ 297 m/pixel at the equator) by using the Generic Mapping Tools' *surface* interpolation routine (Wessel and Smith, 1998) with surface tension set to 0.5, consistent with the currently available Mission Experiment Gridded Data Record products gridded at 128 pixels per degree (Smith et al., 1999b; G. Neumann, 2001, personal commun.).

Gridding the MOLA data to a resolution that approaches the data's sampling interval does introduce a significant fraction of interpolated data between the original spot elevations, which ultimately affects the apparent angles of the forelimb and backlimb

slopes. It is important to note, however, that precise angles of limb slope are not necessary for the slope-asymmetry technique. Only the relative slope magnitudes (i.e., which slope is steeper) need to be noted in order to determine the dip direction of the subjacent thrust. Multiple profiles should be (and are) constructed across a single wrinkle ridge to adequately characterize the sense of slope asymmetry and to reduce possible uncertainties in ridge slope introduced through the gridding process. Furthermore, slope asymmetries evaluated from interpolated high-resolution DEMs have results consistent with the asymmetries taken from obliquely intersecting spot-elevation tracks of the original irregularly spaced PEDR data. Therefore, topographic profiles from high-resolution MOLA-based DEMs can be confidently used to determine the dip directions of faults within thrust-related folds on Mars (Okubo and Schultz, 2004).

APPENDIX 3. MAPPING THRUST-FAULT TRACES

Topographic inversions of the test-case wrinkle ridge show that the upper tips of the subjacent thrusts break the surface or are shallowly buried below the base of the associated fold's forelimb. Therefore at each profile, interpreted dip directions are mapped with a bar and triangle symbol at the base of the corresponding forelimb. Interpreted backthrusts are mapped with white triangle symbols, whereas primary and forethrusts are mapped using a solid black triangle symbol. The bar is aligned parallel with, or tangent to, the local strike of the corresponding fold crest, and the associated triangle points in the downdip direction (Fig. 6A). Finally, a continuous fault trace is created by linking these isolated spot interpretations with a continuous line along the base of the corresponding forelimb (Fig. 6B).

ACKNOWLEDGMENTS

This work is supported by NASA's Planetary Geology and Geophysics Program. We thank G. Stefanelli of the W.M. Keck Earth Sciences and Mining Research Information Center for providing computing support. Reviews by M. Cooke and an anonymous reviewer helped to improve the content of this paper.

REFERENCES CITED

- Albee, A.L., Palluconi, F.D., and Arvidson, R.E., 1998, Mars Global Surveyor Mission: Overview and status: *Science*, v. 279, p. 1671–1672.
- Allemand, P., and Thomas, P., 1992, Brittle deformation model for Martian ridges constrained by surface geometry: *Comptes Rendus de l'Académie des Sciences*, v. 315, p. 1397–1402.
- Anderson, E.M., 1951, The dynamics of faulting and dyke formation, with applications to Britain: Edinburgh, Oliver and Boyd, 206 p.
- Antonellini, M., and Aydin, A., 1994, Effect of faulting on fluid flow in porous sandstones—Petrophysical properties: *American Association of Petroleum Geologists Bulletin*, v. 78, p. 355–377.
- Baratoux, D., Delacourt, C., and Allemand, P., 2002, An instability mechanism in the formation of the Martian lobate craters and the implications for the rheology of ejecta: *Geophysical Research Letters*, v. 29, no. 8, 1210, DOI:10.1029/2001GL013779.
- Barlow, N.G., Koroshetz, J., and Dohm, J.M., 2001, Variations in the onset diameter for Martian layered ejecta morphologies and their implications for subsurface volatile reservoirs: *Geophysical Research Letters*, v. 28, p. 3095–3098.
- Batson, R.M., Bridges, P.M., and Inge, J.L., 1979, Atlas of Mars: NASA Special Publication 438, 146 p.
- Beeman, M., Durham, W.B., and Kirby, S.H., 1988, Friction of ice: *Journal of Geophysical Research*, v. 93, p. 7625–7633.
- Bell, F.G., 1992, *Engineering in rock masses*: Boston, Massachusetts, Butterworth-Heinemann, 580 p.
- Bieniawski, Z.T., 1978, Determining rock mass deformability—Experience from case histories: *International Journal of Rock Mechanics and Mining Sciences*, v. 15, p. 237–247.
- Bieniawski, Z.T., 1989, *Engineering rock mass classifications*: New York, John Wiley, 251 p.
- Bilotti, E., and Suppe, J., 1999, The global distribution of wrinkle ridges on Venus: *Icarus*, v. 139, p. 137–159.
- Bruhn, R.L., and Schultz, R.A., 1996, Geometry and slip distribution in normal fault systems: Implications for mechanics and fault-related hazards: *Journal of Geophysical Research*, v. 101, p. 3401–3412.
- Byerlee, J.D., 1990, Friction, overpressure and fault-normal compression: *Geophysical Research Letters*, v. 17, p. 2109–2112.
- Carr, M.H., Crumpler, L.S., Cutts, J.A., Greeley, R., Guest, J.E., and Masursky, H., 1977, Martian impact craters and emplacement of ejecta by surface flow: *Journal of Geophysical Research*, v. 82, p. 4055–4065.
- Chicarro, A.F., Schultz, P.H., and Masson, P.L., 1985, Global and regional ridge patterns on Mars: *Icarus*, v. 63, p. 153–174.
- Colton, G.W., Howard, K.A., and Moore, H.J., 1972, Mare ridges and arches in southern Oceanus Procellarum: NASA Special Publication 315, p. 29–90–29–93.
- Cooke, M.L., and Pollard, D.D., 1997, Bedding-plane slip in initial stages of fault-related folding: *Journal of Structural Geology*, v. 19, p. 567–581.
- Corbett, K., Friedman, M., and Spang, J., 1987, Fracture development and mechanical stratigraphy of Austin Chalk, Texas: *American Association of Petroleum Geologists Bulletin*, v. 71, p. 17–28.
- Cowie, P.A., and Scholz, C.H., 1992a, Physical explanation for the displacement-length relationship of faults using a post-yield fracture mechanical model: *Journal of Structural Geology*, v. 14, p. 1133–1148.
- Cowie, P.A., and Scholz, C.H., 1992b, Displacement-length scaling relationship for faults: Data synthesis and discussion: *Journal of Structural Geology*, v. 14, p. 1149–1156.
- Croft, S.K., 1980, Cratering flow fields: Implications for the excavation and transient expansion stages of crater formation, in *Proceedings, Lunar and Planetary Science Conference, 11th*: Houston, Lunar and Planetary Institute, p. 2347–2378.
- Crouch, S.L., 1976, Solution of plane elasticity problems by the displacement discontinuity method: *International Journal of Numerical Methods*, v. 10, p. 301–343.
- Crouch, S.L., and Starfield, A.M., 1983, *Boundary element methods in solid mechanics*: Winchester, Massachusetts, Allen and Unwin, 322 p.
- Durham, W.B., Heard, H.C., and Kirby, S.H., 1983, Experimental deformation of polycrystalline H₂O ice at high pressure and low temperature: Preliminary results: *Journal of Geophysical Research*, v. 88, p. B377–B392.
- Dvorkin, J., Mavko, G., and Nur, A., 1999, Overpressure detection from compressional- and shear-wave data: *Geophysical Research Letters*, v. 26, p. 3417–3420.
- Ekström, G., Stein, R.S., Eaton, J.P., and Eberhart-Phillips, D., 1992, Seismicity and geometry of a 110-km-long blind thrust fault: 1. The 1985 Kettleman Hills, California, earthquake: *Journal of Geophysical Research*, v. 97, p. 4843–4864.
- Freed, A.M., and Lin, J., 1998, Time-dependent changes in failure stress following thrust earthquakes: *Journal of Geophysical Research*, v. 103, p. 24,393–24,409.
- Garvin, J.B., Sakimoto, S.E.H., Schnetzler, C., and Frawley, J.J., 1999, Global geometric properties of Martian impact craters: A preliminary assessment using Mars Orbiter Laser Altimeter (MOLA), in *Fifth International Conference on Mars*: Houston, Lunar and Planetary Institute, abstract 6163.
- Golombek, M.P., Plescia, J.B., and Franklin, B.J., 1991, Faulting and folding in the formation of planetary wrinkle ridges, in *Proceedings, Lunar and Planetary Science Conference, 21st*: Houston, Lunar and Planetary Institute, p. 679–693.
- Golombek, M.P., Anderson, F.S., and Zuber, M.T., 2001, Martian wrinkle ridge topography—Evidence for subsurface faults from MOLA: *Journal of Geophysical Research*, v. 106, p. 23,811–23,821.
- Grant, J.A., and Schultz, P.H., 1993, Erosion of ejecta at Meteor Crater, Arizona: *Journal of Geophysical Research*, v. 98, p. 15,033–15,047.
- Gross, M., 1995, Fracture partitioning—Failure mode as a function of lithology in the Monterey Formation of coastal California: *Geological Society of America Bulletin*, v. 107, p. 779–792.
- Gross, M.R., Gutierrez-Alonso, G., Bai, T., Wacker, M.A., and Collinsworth, K.B., 1997, Influence of mechanical stratigraphy and kinematics on fault scaling relations: *Journal of Structural Geology*, v. 19, p. 171–183.
- Hodges, C.A., 1973, Mare ridges and lava lakes: NASA Special Publication 330, p. 31–12–31–21.
- Hoek, E., 1983, Strength of jointed rock masses: *Géotechnique*, v. 33, p. 187–223.
- Hoek, E.T., and Brown, E.T., 1980, Underground excavations in rock: London, Institution of Mining and Metallurgy, 527 p.
- Hoek, E.T., and Brown, E.T., 1997, Practical estimates of rock mass strength: *International Journal of Rock Mechanics and Mining Sciences*, v. 34, p. 1165–1186.
- Howard, K.A., and Muehlberger, W.R., 1973, Lunar thrust faults in the Taurus-Littrow region: NASA Special Publication 330, p. 31–22–31–29.
- Indraratna, B., and Ranjith, P., 2001, Hydromechanical aspects and unsaturated flow in jointed rock: Lisse, Netherlands, A.A. Balkema, 286 p.
- Jaeger, J.C., and Cook, N.G.W., 1979, *Fundamentals of rock mechanics*: London, Chapman and Hall, 593 p.
- King, G., and Yielding, G., 1984, The evolution of a thrust fault system: Processes of rupture initiation, propagation and termination in the 1980 El Asnam (Algeria) earthquake: *Royal Astronomical Society Geophysical Journal*, v. 77, p. 915–933.
- Kreslavsky, M.A., and Basilevsky, A.T., 1998, Morphometry of wrinkle ridges on Venus: Comparison with other planets: *Journal of Geophysical Research*, v. 103, p. 11,103–11,111.
- Kulhawy, F.H., 1975, Stress-deformation properties of rock and rock discontinuities: *Engineering Geology*, v. 9, p. 327–350.
- Lin, J., and Stein, R.S., 1989, Coseismic folding, earthquake recurrence and the 1987 source mechanism at Whittier Narrows, Los Angeles Basin, California: *Journal of Geophysical Research*, v. 94, p. 9614–9632.
- Mair, K., Frye, K.M., and Marone, C., 2002, Influence of grain characteristics on the friction of granular shear zones: *Journal of Geophysical Research*, v. 107, no. B10, 2219, DOI:10.1029/2001JB000516.
- Mangold, N., Allemand, P., and Thomas, P.G., 1998, Wrinkle ridges of Mars—Structural analysis and evidence for shallow deformation controlled by ice-rich décollements: *Planetary and Space Science*, v. 46, p. 345–356.
- Manzocchi, T., Ringrose, P.S., and Underhill, J.R., 1998, Flow through fault systems in high-porosity sandstones, in *Coward, M.P., Daltban, T.S., and Johnson, H., eds., Structural geology in reservoir characterization*: Geological Society [London] Special Publication 127, p. 65–82.
- Mase, C.W., and Smith, L., 1987, Effects of frictional heating on the thermal, hydrologic, and mechanical response of a fault: *Journal of Geophysical Research*, v. 92, p. 6249–6272.
- Melosh, H.J., 1989, *Impact cratering: A geologic process*: New York, Oxford University Press, 245 p.
- Mercier, E., Outtani, F., and de Lamotte, D.F., 1997, Late-stage evolution of fault-propagation folds—Principles and example: *Journal of Structural Geology*, v. 19, p. 185–193.
- Morrow, C.A., Moore, D.E., and Lockner, D.A., 2000, The effect of mineral bond strength and absorbed water on

- fault gouge frictional strength: *Geophysical Research Letters*, v. 27, p. 815–818.
- Mouginis-Mark, P., 1979, Martian fluidized crater morphology—Variations with crater size, latitude, altitude and target material: *Journal of Geophysical Research*, v. 84, p. 8011–8022.
- Neumann, G.A., Rowlands, D.D., Lemoine, F.G., Smith, D.E., and Zuber, M.T., 2001, The crossover analysis of MOLA altimetric data: *Journal of Geophysical Research*, v. 106, p. 23,753–23,768.
- Niño, F., Philip, H., and Chéry, J., 1998, The role of bed-parallel slip in the formation of blind thrust faults: *Journal of Structural Geology*, v. 20, p. 503–516.
- Okubo, C., and Schultz, R., 2002, What can the topography of thrust-related anticlines tell us about mechanical stratigraphy and pore fluid pressure?: *Eos (Transactions, American Geophysical Union)*, v. 83, Fall Meeting Supplement, abstract T12G-01, p. F1365.
- Okubo, C., and Schultz, R., 2003, Fault-controlled fluid seep potential and surface strength at the Isidis and Elysium Planitia MER sites based on numerical modeling of wrinkle ridge topography: *Lunar and Planetary Science Conference*, 34th, abstract 1484.
- Okubo, C.H., and Schultz, R.A., 2004, Gridding Mars Orbiter Laser Altimeter data with GMT: Effects of pixel size and interpolation methods on DEM integrity: *Computers and Geosciences*, v. 30 (in press).
- Okubo, C., Schultz, R., Cooke, M., and Lin, J., 2001, Brittle strain localization and thrust fault geometry within thrust cored folds: Causative principal stresses and insights from Coulomb stress change: *Eos (Transactions, American Geophysical Union)*, v. 82, Fall Meeting Supplement, abstract T51A-0851, p. F1230.
- Parry, W.T., 1998, Fault-fluid compositions from fluid-inclusion observations and solubilities of fracture-sealing minerals: *Tectonophysics*, v. 290, p. 1–26.
- Peacock, D.C.P., and Zhang, X., 1994, Field examples and numerical modeling of oversteps and bends along normal faults in cross-section: *Tectonophysics*, v. 234, p. 147–168.
- Priest, S.D., 1993, *Discontinuity analysis for rock engineering*: London, Chapman and Hall, 473 p.
- Roering, J.J., Cooke, M.L., and Pollard, D.D., 1997, Why blind thrust faults do not propagate to the Earth's surface—Numerical modeling of coseismic deformation associated with thrust-related anticlines: *Journal of Geophysical Research*, v. 102, p. 11,901–11,912.
- Saffer, D.M., Frye, K.M., Marone, C., and Mair, K., 2001, Laboratory results indicating complex and potentially unstable frictional behavior of smectite clay: *Geophysical Research Letters*, v. 28, p. 2297–2300.
- Schultz, R.A., 1992, Mechanics of curved slip surfaces in rock: *Engineering Analysis with Boundary Elements*, v. 10, p. 147–154.
- Schultz, R.A., 1996, Relative scale and the strength and deformability of rock masses: *Journal of Structural Geology*, v. 18, p. 1139–1149.
- Schultz, R.A., 2000, Localization of bedding plane slip and backthrust faults above blind thrust faults: Keys to wrinkle ridge structure: *Journal of Geophysical Research*, v. 105, p. 12,035–12,052.
- Schultz, R.A., and Aydin, A., 1990, Formation of interior basins associated with curved faults in Alaska: *Tectonics*, v. 9, p. 1387–1407.
- Schultz, R.A., and Lin, J., 2001, Three-dimensional normal faulting models of Valles Marineris, Mars, and geodynamic implications: *Journal of Geophysical Research*, v. 106, p. 16,549–16,566.
- Schultz, R.A., and Watters, T.R., 2001, Forward mechanical modeling of the Amenthes Rupes thrust fault on Mars: *Geophysical Research Letters*, v. 28, p. 4659–4662.
- Scott, D.H., and Tanaka, K.L., 1986, Geologic map of the western equatorial region of Mars: U.S. Geological Survey Miscellaneous Geologic Investigations Series Map I-1802-A, scale 1:15,000,000, 1 sheet.
- Sibson, R.H., Moore, J.M., and Rankin, A.H., 1975, Seismic pumping—A hydrothermal fluid transport mechanism: *Geological Society [London] Journal*, v. 131, p. 653–659.
- Sleep, N.H., 1995, Frictional heating and the stability of rate and state dependent frictional sliding: *Geophysical Research Letters*, v. 22, p. 2785–2788.
- Smith, D.E., Neumann, G.A., Ford, P.G., Arvidson, R.E., Guinness, E.A., and Slavney, S., 1999a, Mars Global Surveyor Laser Altimeter Precision Experiment Data Record: MGS-M-MOLA-3-PEDR-L1A-V1.0: NASA Planetary Data System.
- Smith, D.E., Neumann, G.A., Ford, P.G., Arvidson, R.E., Guinness, E.A., and Slavney, S., 1999b, Mars Global Surveyor Laser Altimeter Precision Experiment Data Record: MGS-M-MOLA-5-MEGDR-L3-V1.0: NASA Planetary Data System.
- Stein, R.S., and Ekström, G., 1992, Seismicity and geometry of a 110-km-long blind thrust fault: 2. Synthesis of the 1982–1985 California earthquake sequence: *Journal of Geophysical Research*, v. 97, p. 4865–4883.
- Stewart, S.T., O'Keefe, J.D., and Ahrens, T.J., 2001, The relationship between rampart crater morphologies and the amount of subsurface ice, *in Abstracts, Lunar and Planetary Science Conference*, 22nd: Houston, Lunar and Planetary Institute, abstract 2092.
- Stone, D.S., 1999, Foreland basement-involved structures—Discussion: *American Association of Petroleum Geologists Bulletin*, v. 83, p. 2006–2016.
- Strayer, L.M., Hudleston, P.J., and Lorig, L.J., 2001, A numerical model of deformation and fluid-flow in an evolving thrust wedge: *Tectonophysics*, v. 335, p. 121–145.
- Suppe, J., 1985, *Principles of structural geology*: Englewood Cliffs, New Jersey, Prentice-Hall, 537 p.
- Taboada, A., Bousquet, J.C., and Philip, H., 1993, Coseismic elastic models of folds above blind thrusts in the Betic Cordilleras (Spain) and evaluation of seismic hazard: *Tectonophysics*, v. 220, p. 223–241.
- Tanaka, K.L., Skinner, J.A., Hare, T.M., Joyal, T., and Wenker, A., 2003, Resurfacing history of the northern plains of Mars based on geologic mapping of Mars Global Surveyor data: *Journal of Geophysical Research*, v. 108, no. E4, 8043, DOI:10.1029/2002JE001908.
- Travé, A., Labaume, P., Calvet, F., and Soler, A., 1997, Sediment dewatering and pore fluid migration along thrust faults in a foreland basin inferred from isotopic and elemental geochemical analyses (Eocene southern Pyrenees, Spain): *Tectonophysics*, v. 282, p. 375–398.
- Urrutia-Fucugauchi, J., Marin, L., and Trejo-García, A., 1996, UNAM scientific drilling program of Chicxulub impact structure—Evidence for a 300 kilometer crater diameter: *Geophysical Research Letters*, v. 23, p. 1565–1568.
- Watters, T.R., 1988, Wrinkle ridge assemblages on the terrestrial planets: *Journal of Geophysical Research*, v. 93, p. 10,236–10,254.
- Watters, T.R., and Maxwell, T.A., 1986, Orientation, relative age, and extent of the Tharsis Plateau ridge system: *Journal of Geophysical Research*, v. 91, p. 8113–8125.
- Watters, T.R., and Robinson, M.S., 1997, Radar and photogrammetric studies of wrinkle ridges on Mars: *Journal of Geophysical Research*, v. 102, p. 10,889–10,903.
- Wessel, P., and Smith, W.H.F., 1998, New, improved version of Generic Mapping Tools released: *Eos (Transactions, American Geophysical Union)*, v. 79, p. 579.
- Wu, Fa-quan, and Wang, Si-jing, 2001, A stress-strain relation for jointed rock masses: *International Journal of Rock Mechanics and Mining Sciences*, v. 38, p. 591–598.
- Young, R.A., Brennan, W.J., Wolfe, R.W., and Nichols, D.J., 1973, Volcanism in the Lunar maria: *NASA Special Publication* 330, p. 31–11.
- Zuber, M.T., Smith, D.H., Solomon, S.C., Muhleman, D.O., Head, J.W., Garvin, J.B., Abshire, J.B., and Bufton, J.L., 1992, The Mars Observer Laser Altimeter investigation: *Journal of Geophysical Research*, v. 97, p. 7781–7797.

MANUSCRIPT RECEIVED BY THE SOCIETY 24 MARCH 2003

REVISED MANUSCRIPT RECEIVED 6 AUGUST 2003

MANUSCRIPT ACCEPTED 10 SEPTEMBER 2003

Printed in the USA